CAMBRIDGE
UNIVERSITY PRESS

Article

Polygenic chamosite from a hydrothermalized oolitic ironstone (Saint-Aubin-des-Châteaux, Armorican Massif, France): crystal chemistry, visible–near-infrared spectroscopy (red variety) and geochemical significance

Yves Moëlo[1]* (ID), Emmanuel Fritsch[1], Eric Gloaguen[2,3] and Olivier Rouer[4]

[1]Université de Nantes, CNRS, Institut des Matériaux Jean Rouxel, IMN, F-44000 Nantes, France; [2]BRGM, 3, avenue Claude Guillemin, BP 36009, 45060 Orléans cedex 2, France; [3]ISTO, UMR 7327, Université d'Orléans, CNRS, BRGM, F-45071 Orléans, France and [4]Laboratoire Georessources, UMR 7359, FST-SCMEM, Université de Lorraine, BP 70239-54506 Vandœuvre les Nancy Cedex, France

Abstract

Several generations of chamosite, including a red variety, occur in the Ordovician hydrothermalized oolitic ironstone from Saint-Aubin-des-Châteaux (Armorican Massif, France). Their chemical re-examination indicates a low Mg content ($0.925 < Fe/(Fe + Mg) < 0.954$), but a significant variation in ^{IV}Al. Minor vanadium is present at up to 1.1 wt.% oxide. Variations in ^{IV}Al, the vanadium content and the colour of chamosite are related to the hydrothermal reworking of the ironstone. Taking into account other published data, the ideal composition of chamosite is $(Fe_{5-x}Al_{1+x})(Si_{3-x}Al_{1+x})O_{10}(OH)_8$, with $0.2 < x < 0.8$ (0.2: equilibrium with quartz; 0.8: SiO_2 deficit). The red chamosite (IIb polytype) has a mean composition of $(Fe_{3.87}Mg_{0.23}Mn_{0.01}\square_{0.07}Al_{1.74}V_{0.07})(Si_{2.33}Al_{1.67})O_{10}(OH)_8$. This chamosite is strongly pleochroic, from pale yellow ($\mathbf{E} \parallel (001)$) to deep orange red ($\mathbf{E} \perp (001)$). Visible–near-infrared absorbance spectra show a specific absorption band centred at ∼550 nm for $\mathbf{E} \perp (001)$, due to a proposed new variety of Fe/V intervalence charge-transfer mechanism in the octahedral sheet, possibly $Fe^{2+} – V^{4+} \rightarrow Fe^{3+} – V^{3+}$. While the formation of green chamosite varieties is controlled by reducing conditions due to the presence of organic matter as a buffer, that of red chamosite would indicate locally a weak increase of f_{O_2} related to oxidizing hydrothermal solutions.

In the sandstone quarry of Saint-Aubin-des-Châteaux (Loire-Atlantique department, Armorican Massif, France), an Ordovician oolitic ironstone (Chauvel, 1971 & 1974) contains, together with ordinary green chlorite, a striking variety of 'red chlorite', observed in the past during petrographic studies (G. Cornen, pers. comm.), which was characterized later as an Mg-poor chamosite (Gloaguen et al., 2007). Gloaguen et al. (2007) established various chamosite generations and provided an opportunity for their detailed chemical study. In addition, an optical study was performed on the red chamosite to interpret its location within the sequence of chamosite generations and the origin of its colour.

At Saint-Aubin-des-Châteaux, the oolitic ironstone was subjected to very-low-grade metamorphism (anchizone) and is mainly composed of siderite and chamosite, with abundant organic matter (vitrinite reflectance $R = 3.9 \pm 0.2\%$). Later, this ironstone was hydrothermally altered by early Variscan polyphase fluid flow (Gloaguen et al., 2007; Tartèse et al., 2015) related to a 360 Ma mafic magmatism (Pochon et al., 2016a, 2016b). This fluid flow induced specific mineralizations (Pochon et al., 2017, 2018),

including the Saint-Aubin-des-Châteaux sulfide ore (Pochon et al., 2019). In this deposit, the oolitic ironstone was partly transformed into pyritized lenticular bodies and associated chlorite alteration haloes. It was followed by additional fracturing stages that trapped base metals (Pb, Zn, Cu, Sb and minor Au). This hydrothermal process led to a peculiar mineralogy, highlighted by the formation of lulzacite $Sr_2Fe^{2+}(Fe^{2+}, Mg)_2Al_4(PO_4)_4(OH)_{10}$ (type locality; Moëlo et al., 2000), pretulite $ScPO_4$ (Moëlo et al., 2002), tobelite $((NH_4),K)Al_2(Si_3Al)O_{10}(OH)_2$ (Mesto et al., 2012; Capitani et al., 2016; Pochon et al., 2019) and Sr-rich apatite with rare earth element (*REE*) phosphates (Moëlo et al., 2008).

The hydrothermal process was controlled by three geochemical reactions:

1. Leaching of siderite by acid solutions, which were neutralized.
2. Sulfidation (pyritization) by combination of Fe from dissolved siderite with sulfur transported by the solution.
3. Redox processes: oxidation of partly dissolved organic matter with re-precipitation of minor graphite lamellae. Conversely, the hydrothermal solution was reduced.

As a whole, this process may be similar to the process of thermochemical sulfate reduction considered in the formation of Mississippi Valley-type lead–zinc ores (Leach et al., 2010).

*E-mail: Yves.Moelo@cnrs-imn.fr

There are several generations of chamosite in the Saint-Aubin deposit (Table 1) (Gloaguen *et al.*, 2007). Primary chamosite (green), the most abundant variety, is the main constituent, together with the siderite cement of primitive oolites in the sedimentary iron ore (ooidal ironstone), caused by diagenesis and low-grade metamorphism (Chauvel, 1971, 1974). Other chamosite generations (green and red) are related to stages 1–3 of the hydrothermal process in various ore facies (Table 1). The red chamosite is associated closely with the sulfide ore (stages 1 and 2). It has also been observed as isolated crystals disseminated in an apatite-rich sample, together with crystals of pretulite ($ScPO_4$). Hydrothermal green chamosite has been observed in stage 1 (chlorite–pyrite facies; chlorite-rich reaction rim), stage 2 (lulzacite-bearing quartz–siderite veinlets; polymetallic quartz veins within sandstones) and stage 3 (tobelite–sulfosalt–gold quartz veins within sandstones).

According to Gloaguen *et al.* (2007), using chlorite as a geothermometer gives a formation temperature of ~290°C for metamorphic chamosite, followed by a T increase (~310–340°C) for stage 1, then T decreases for stage 2 (~300°C) and stage 3 (~275°C). Of particular interest is the late formation (stage 4) of berthierine, the 7 Å low-T dimorph of chamosite, also with an unusual brown colour (Moëlo *et al.*, 2006), associated with quartz, minor kaolinite and Eu-enriched apatite (Moëlo *et al.*, 2008).

In the present study, the first section is devoted to the crystal chemical re-examination of the various chamosite generations, taking into account the first electron probe microanalyses (EPMAs) of Gloaguen *et al.* (2007), complemented by new EPMAs. The second section is focused on the spectroscopic study of red chamosite to characterize its absorption bands in the visible–near-infrared (Vis–NIR) range. In the third section, a comparison of these data and geochemical constraints provides useful indications on the evolution of the chamosite composition and on the origin of the red colour of chamosite. We propose that such a colour originates from a new intervalence charge-transfer (IVCT) mechanism involving minor vanadium together with the main iron.

Brief review of chlorite crystal chemistry

Chlorites are phyllosilicates with a 14 Å layer spacing, where a talc-like sheet $^{VI}(R^{2+},R^{3+})_3{}^{IV}(Si,R^{3+})O_{10}(OH)_2$ alternates with a brucite sheet $^{VI}(R^{2+},R^{3+})_3(OH)_6$ (Brown & Bailey, 1962). The cation R^{2+} is mainly Mg and Fe^{2+}, and R^{3+} is mainly Al and Fe^{3+}. ^{VI}R and ^{IV}R correspond to octahedral and tetrahedral cations, respectively. Taking into account possible vacancies ($\square$), their general structural formula is $^{VI}(R^{2+}{}_{6-y-z}R^{3+}{}_y\square_z)^{IV}(Si_{4-x}R^{3+}{}_x)O_{10}(OH)_8$ (Bailey, 1980). For charges to be balanced, $y = x + 2z$.

Clinochlore is the Mg species containing mainly Mg^{2+} and Al^{3+}, with the ideal formula $(Mg_5Al)(Si_3Al)O_{10}(OH)_8$ (no vacancy: purely trioctahedral). Chamosite is the Fe^{2+} endmember, with the ideal formula $(Fe_5Al)(Si_3Al)O_{10}(OH)_8$ proposed by Bayliss (1975). The crystal chemical classification of chlorites by Wiewióra & Weiss (1990) also takes into account the vacancy content as well as the Tschermak substitution rule $^{VI}R^{2+} + {}^{IV}Si^{4+} \leftrightarrow {}^{VI}Al^{3+} + {}^{IV}Al^{3+}$. Recently, Trincal & Lanari (2016) proposed a new substitution rule, correlating Fe^{3+} and vacancy: $3(Mg,Fe)^{2+} \rightarrow 2Fe^{3+} + \square$.

Chlorites show six polytypic groups (Bailey, 1988; Inoué & Kogure, 2016), with various types of stacking disorder (Brindley, 1980). Interstratification with other phyllosilicates, minerals of the serpentine group as well as smectite is common. In particular,

Table 1. Various generations of chamosite in Saint-Aubin-des-Châteaux.

Stage	Ore type	Ch. col.	No.
Weak metamorphic	Oolitic	Green	1
Hydrothermal HT 1	Oolitic + chamosite	Green	2
	Chamosite + pyrite	Green	3
	Replacement front with chamosite + apatite[a]	Red	4–5
	Replacement front with chamosite	Green	6
	Massive sulfide lens	Red	7
Hydrothermal HT 2	Edge of sulfide vein	Red	8–11
Hydrothermal HT 3	Polymetallic quartz vein within sandstone	Green	12
	Quartz + pyrite + siderite + Lz vein	Green	13
	Quartz + Tob + SFS + Au vein within sandstone	Green	14
	Sandstone	Green	15–16
Late hydrothermal LT 4	Retromorphosis – berthierine[b]	Brown	17

[a]Source of single crystal for XRD analysis.
[b]7 Å dimorph of chamosite.
Ch. col. = chamosite colour; HT = high temperature; LT = low temperature; Lz = lulzacite; No.: analysis number in Tables 2 & 3; SFS = sulfosalts; Tob = tobelite.

interstratification between chamosite and berthierine is commonly observed (Jiang *et al.*, 1992; Inoué & Kogure, 2016).

In the clinochlore–chamosite solid solution, the relationships between the chemistry and the unit cell are controlled by several factors:

1. A steric factor due to Fe substituting for Mg: the increase of $^{IV}Al^{3+}$ with that of the Fe:(Fe + Mg) ratio obeys steric constraints (Shau & Peacor, 1992). The expansion of the octahedral sheets due to the Fe-for-Mg substitution induces an expansion of the tetrahedral sheets obtained through the Al^{3+}-for-Si^{4+} substitution.
2. Charge balance: this second substitution corresponds to a charge deficit, which ought to be compensated by a charge increase in the octahedral sheet, according to the Al^{3+}-for-Me^{2+} substitution. This retroactive effect reduces the expansion of the octahedral sheet: for one Al atom substituting one Si atom among four tetrahedral positions, one Al atom substitutes one Me^{2+} among six octahedral positions. This Tschermak substitution explains the abnormal slight c decrease with increasing Fe:(Fe + Mg) ratio (Hey, 1954; McOnie *et al.*, 1975).
3. Phase equilibrium: at constant Fe:(Fe + Mg) ratio, the Tschermak substitution may also operate for a second time according to the Al:Si ratio of the system. An SiO_2 excess will impose a low ^{IV}Al, whereas an SiO_2 deficit will result in a high ^{IV}Al, as is documented in Saint-Aubin.
4. Vacancies in the octahedral sheets, according to the dioctahedral substitution $3Me^{2+} \rightarrow 2Me^{3+} + \square$, will induce a contraction of these sheets, and thus counterbalance the expansion due to Fe/Mg substitution.

In the present study, two stoichiometric compositions (Mg and vacancy free) have been taken as references for discussing the chamosite crystal chemistry: the first being Al poor, $(Fe_5Al)(Si_3Al)O_{10}(OH)_8$, frequently encountered in mineralogical databases, and the second being Al rich, $(Fe_4Al_2)(Si_2Al_2)O_{10}(OH)_8$.

Materials and analytical methods

Polished thin sections and polished sections for microscopic study, EPMA and optical study were prepared from selected

chamosite-bearing samples. Additionally, isolated single crystals of red chamosite were extracted from an apatite-rich sample for X-ray examination. Samples were first observed under a binocular loupe and through a polarizing microscope (in transmitted and reflected light) to select chamosite varieties and to determine their mineral associations (Table 1).

Electron probe microanalysis

All EPMA data were obtained at the BRGM-CNRS-University common laboratory (Orléans), with a CAMECA SX50 apparatus with a voltage of 15 kV and a beam current of 12 nA. Analysed elements were (all with $K\alpha$ emission lines; standards indicated in parentheses): Fe (Fe_2O_3), Mn (Mn_2O_3), Mg (olivine), Al (albite), V (vanadinite), Si (albite) and Ti ($MnTiO_3$). Minor elements (≤ 0.1 wt.% oxide) detected by Gloaguen *et al.* (2007) but not essential in the crystal chemistry of chlorite (*i.e.* Ca, Ba, Zn, Cu, K, Na, F, Cl) have been omitted. H_2O content (wt.%) has been added on the basis of 4 H_2O for 14 O of the oxide total to fit the $O_{10}(OH)_8$ ratio of the structural formula.

X-ray diffraction study

The dissemination of red chamosite in the sulfide ore precluded obtaining a precise X-ray diffraction (XRD) trace, which would establish its polytype and thus detect possible interstratification with berthierine, as is commonly observed in chamosite from hydrothermal ores (Inoué & Kogure, 2016). Nevertheless, dissolution in hydrochloric acid of abundant apatite in a pretulite-bearing sample made it possible to extract single crystals of red chamosite. One crystal was mounted on a glass capillary for a single-crystal XRD study with STOE-IPDS diffractometer (Image Plate Diffraction System) using Mo-$K\alpha$ radiation (operator: A. Meerschaut, Institut des Matériaux de Nantes).

Optical microscopy study

The optical microscopy study was focused on pure red chamosite, without the neighbouring green variety. Thin sections containing red chamosite crystals were investigated with visible light (410–760 nm). Transmitted spectra have been acquired using a LEICA DMR polarizing microscope equipped with a MPV-SP microphotometer. The bandwidth of the monochromator was $\Delta\lambda = 2$ nm. Computation of colour values and their representation in a chromaticity diagram were performed according to the protocol detailed by Criddle (1990, and references therein), taking illuminant C source ('average daylight' – colour temperature 6774 K) of the Commission Internationale de l'Eclairage (CIE) as the standard for white colour.

The absorption spectra in the Vis–NIR range (340–2500 nm; *i.e.* 29 400–4000 cm^{-1}) have been acquired in transmitted light on the same thin sections (standard thickness of 30 μm). A Varian Cary 5000 double-beam absorption spectrophotometer was used with a sampling interval of 1 nm and a 1 nm spectral bandwidth. The sample measured was a thin section of a red chamosite lamella with the polarization direction parallel or perpendicular to the elongation of the lamella. The glass and glue support were compensated by a similar setup on the reference beam: a standard glass slab for lithographic thin section, as was used for the sample, was covered on a region larger than the UV–Vis beam section with the same glue. This was then turned into a very thin bevel to offer all possible equivalents of glue thickness, and then the position

of the bevel in the beam was adjusted to compensate for a potential small glue contribution, which is rare.

Results

Electron probe microanalyses

Table 2 shows the EPMA data as wt.% oxides with divalent Fe and Mn and trivalent V according to the strongly reducing conditions indicated by the abundance of organic matter in the primitive oolitic iron ore and the presence of ammonium–mica (tobelite). Table 3 indicates the structural formulae on the basis of $O_{10}(OH)_8$ as the anionic counterpart.

Main components
Figure 1a represents analyses as ^{IV}Al *vs* Fe:(Fe + Mg) ratios. As indicated first by Chauvel (1971) and further demonstrated by Gloaguen *et al.* (2007), Fe largely predominates over Mg (Fe:Mg >12) in Saint-Aubin chlorites. The majority of analyses are restricted to an Fe:(Fe + Mg) ratio close to 0.946 (±0.006). By contrast, there is significant variation of ^{IV}Al (*i.e.* of the Tschermak substitution rule) from 1.41 up to 1.80 atoms per $O_{10}(OH)_8$.

Vacancies
Table 3 shows a small number of vacancies of between 0.005 and 0.170 octahedral sites per $O_{10}(OH)_8$. Figure 1b represents the projection of chamosite compositions on the diagram Si *vs* Me^{2+} according to Wiewióra & Weiss (1990), as used by Hillier & Velde (1991). This diagram visualizes the vacancy concentration.

Trivalent Fe
Fe^{3+} may significantly substitute for $^{VI}Al^{3+}$, such as in 'orthochamosite' (Novak *et al.*, 1959), with ideal composition $((Fe^{2+},Mg,Fe^{3+})_5Al)(Si_3Al)O_{10}(OH,O)_8$. Nevertheless, the EPMA did not reveal minor Fe^{3+} in chamosite from Saint-Aubin.

Distribution of minor transition metals
Together with major iron, V, Mn and Ti are the three transition metals detected as minor constituents (Tables 2 & 3). Zn and Cu, rarely detected by Gloaguen *et al.* (2007) (maxima 0.12 and 0.04 wt.% oxide, respectively) in chamosite from stage 1, may correspond to sulfide contamination. The Ti content is always very low (≤ 0.03 wt.% oxide) and that of Mn is slightly higher (0.06–0.29 wt.% oxide).

By contrast, the vanadium content is more heterogeneous (Gloaguen *et al.*, 2007) and may reach >1 wt.% oxide. Vanadium zoning can be observed. For instance, the centre of a lamella of red chamosite (No. 10, Table 2) is enriched with V and Al relative to the rim (No. 11, Table 2). Correlatively, Mn and Ti, both with very small contents (Table 2), increase slightly.

Late brown berthierine, formed at low temperatures at the expense of lulzacite (0.64 wt.% V_2O_5; Moëlo *et al.*, 2000), also contains minor V (0.46 wt.% V_2O_3; Table 2). Mn and Ti are negligible. In equilibrium with kaolinite and quartz, berthierine has the Al-poor composition $(Fe_{3.90}Mg_{0.24}\square_{0.15}Al_{1.67}V_{0.04})(Si_{2.56}Al_{1.44})O_{10}(OH)_8$, which is very close to that of late green chamosite No. 16 (Table 3).

Crystallography

The single-crystal XRD analysis of red chamosite (No. 5, Tables 2 & 3) yielded a monoclinic unit cell, space group $C2/m$, with
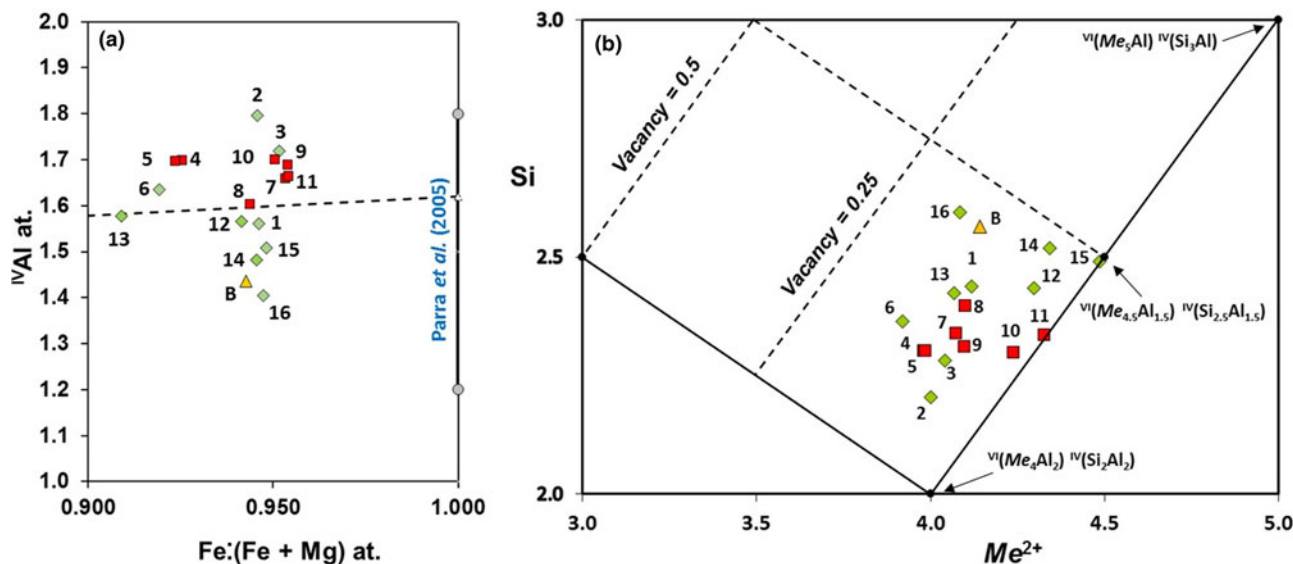
Fig. 1. Analyses of chamosite varieties from Saint-Aubin according to Tables 2 & 3: (a) ^{IV}Al *vs* Fe:(Fe + Mg) atom diagram; (b) Si *vs* Me^{2+} atom diagram (Wiewióra & Weiss, 1990). Dashed line in (a) is the regression curve for metamorphic chlorites (Zane *et al.*, 1998). Red squares: orange-red chamosite; green diamonds: oolitic and hydrothermal green chamosite; yellow triangle: associated berthierine (B – No. 17). Si and Me^{2+} refer to the cation number per $O_{10}(OH)_8$. $Me^{2+} = Mg^{2+} + Fe^{2+}$.

Table 2. Electron probe microanalysis of various chamosite generations from Saint-Aubin in terms of wt.% oxides.

No.	Colour	FeO	MnO	MgO	Al_2O_3	V_2O_3	SiO_2	TiO_2	Sum	$+H_2O$
1^a	Green	40.12	0.11	1.28	24.25	0.25	21.05	0.02	87.08	97.38
2^a	Green	40.05	0.07	1.29	27.69	0.47	19.54	0.02	89.13	99.71
3^a	Green	40.00	0.06	1.14	26.48	0.10	19.87	0.03	87.68	98.07
4^a	Red	39.09	0.06	1.77	26.66	0.82	20.46	0.01	88.87	99.48
5	Red	39.12	0.06	1.82	26.66	0.83	20.50	0.01	88.99	99.61
6^a	Green	37.98	0.17	1.87	26.20	0.84	20.93	0.02	88.01	98.58
7^a	Red	40.71	0.11	1.12	25.50	0.84	20.57	0.02	88.87	99.36
8^a	Red	40.30	0.10	1.35	25.05	0.24	20.93	0.01	87.98	98.40
9	Red	41.60	0.12	1.13	26.06	0.88	20.63	0.01	90.43	101.09
10	Red	42.36	0.06	1.24	25.00	1.06	20.25	0.01	89.97	100.48
11	Red	42.77	0.08	1.16	24.13	0.58	20.28	0.03	89.03	99.39
12^a	Green	38.79	0.29	2.18	25.39	0.02	21.41	0.01	88.09	98.78
13	Green	42.35	0.12	1.48	23.95	0.02	21.36	0.04	89.31	99.64
14^a	Green	42.34	0.15	1.37	22.58	0.03	21.79	0.02	88.28	98.61
15	Green	43.97	0.00	1.35	21.89	0.38	21.54	0.02	89.16	99.48
16	Green	41.06	0.00	1.28	23.44	0.39	23.03	0.03	89.22	99.82
17^b	Red	41.74	0.01	1.42	23.59	0.46	22.94	0.02	90.18	100.85

^{a}First set of analyses (Gloaguen *et al.*, 2007).
^{b}Late berthierine (for comparison).

$a = 5.375(1)$, $b = 9.322(2)$, $c = 14.177(3)$ Å, $\beta = 97.43(3)°$ and $V = 704.4$ Å^3. The structural formula of chamosite is $Fe_{3.68}Mg_{0.30}Mn_{0.01}\square_{0.11}Al_{1.83}V_{0.08})(Si_{2.30}Al_{1.70})O_{10}(OH)_8$ (Tables 2 & 3). This formula most closely corresponds to polytype II*b*, the most common chlorite polytype (Brown & Bailey, 1962). Thus, although the relatively poor quality of the XRD trace was not suitable for detailed crystal structure investigation, it is safe to assume a II*b* polytype for the red chamosite.

Optical study of red chamosite

Visible transmission spectra

Under the binocular loupe, submillimetric individual crystals of red chamosite present a brown colour. In thin section, red chamosite observed under the microscope with polarized light shows a

very strong pleochroism, from near-white to deep orange-red (Fig. 2). This pleochroism is of the normal type (Richardson & Richardson, 1982); in other words, the selective absorption giving the strong colouring is maximal when the polarization plane is parallel to the elongation of the chamosite lamella ($E \parallel (001)$).

Figure 3 presents the two visible transmittance spectra obtained with the polarization plane perpendicular (A, blue line) or parallel (B, red line) to the lamella plane, respectively. In A ($E \perp (001)$), the transmittance is highest in the middle of the spectrum (560–620 nm), with a regular decrease down to ~50% at the two ends of the spectrum. Conversely, in B ($E \parallel (001)$), no transmittance is observed from 420 to 540 nm; a weak transmittance window (~40%) is centred near 700 nm. These data show the very strong absorption for $E \parallel (001)$.

In the chromaticity diagram (Fig. 4), the chromaticity coordinates of the A and B spectra are $x_C = 0.34$, $y_C = 0.36$ and $x_C = 0.63$, $y_C = 0.33$, respectively. Point A, close to the CIE illuminant C (white daylight), corresponds to a pale yellow hue (dominant wavelength $\lambda_D = 572$ nm; excitation purity $P_e \approx 15\%$), while point B corresponds to a saturated orange-red hue ($\lambda_D = 610$ nm; $P_e \approx 90\%$).

Vis–NIR absorbance spectra

The two preceding transmitted-light spectra correspond to the left half of Part I of Fig. 5, which presents the two Vis–NIR absorbance spectra of red chamosite: A (blue 'perpendicular'; $E \perp (001)$) and B (red 'parallel'; $E \parallel (001)$). All well-defined absorption bands as well as some possible minor ones have been indexed, and these are listed in Table 4. These Vis–NIR spectra can be divided in to two regions:

1. Region I (from 340 to 1350 nm) is dominated by electronic transitions. In A, it shows a strong complex absorption band between 650 and 1350 nm, together with a continuum rising towards the UV range. The complex band is the sum of a main band at ~915 nm, with a second band at ~1100 nm. The continuum shows possibly very weak bands at ~460, 605 and 645 nm. In B, the two main components of the complex band are centred at

Table 3. Electron probe microanalysis of various chamosite generations from Saint-Aubin in terms of cation contents per $O_{10}(OH)_8$.

No.	Colour	Fe	Mn	Mg	Al	V	Si	^{IV}Al	^{VI}Al	ΣMe	Vac.	Fe rat.
1	Green	3.89	0.01	0.22	3.31	0.02	2.44	1.56	1.75	9.89	0.11	0.944
2	Green	3.78	0.01	0.22	3.68	0.04	2.20	1.80	1.89	9.93	0.07	0.944
3	Green	3.84	0.01	0.20	3.58	0.01	2.28	1.72	1.87	9.92	0.08	0.950
4	Red	3.68	0.01	0.30	3.53	0.07	2.30	1.70	1.84	9.89	0.11	0.924
5	Red	3.68	0.01	0.30	3.53	0.08	2.30	1.70	1.83	9.89	0.11	0.922
6	Green	3.59	0.02	0.31	3.49	0.08	2.36	1.64	1.85	9.85	0.15	0.916
7	Red	3.87	0.01	0.19	3.42	0.08	2.34	1.66	1.86	9.91	0.09	0.951
8	Red	3.86	0.01	0.23	3.38	0.02	2.40	1.60	1.78	9.90	0.10	0.941
9	Red	3.90	0.01	0.19	3.44	0.08	2.31	1.69	1.75	9.93	0.07	0.951
10	Red	4.02	0.01	0.21	3.34	0.10	2.30	1.70	1.64	9.98	0.02	0.949
11	Red	4.12	0.01	0.20	3.28	0.05	2.34	1.66	1.61	10.00	0.00	0.952
12	Green	3.67	0.03	0.37	3.39	0.00	2.42	1.58	1.81	9.88	0.12	0.903
13	Green	4.04	0.01	0.25	3.22	0.00	2.43	1.57	1.65	9.95	0.05	0.939
14	Green	4.09	0.01	0.24	3.08	0.00	2.52	1.48	1.59	9.94	0.06	0.942
15	Green	4.25	0.00	0.23	2.98	0.04	2.49	1.51	1.47	10.00	0.00	0.948
16	Green	3.87	0.00	0.22	3.11	0.04	2.59	1.41	1.71	9.83	0.17	0.947
17^a	Red	3.90	0.00	0.24	3.11	0.04	2.56	1.44	1.67	9.86	0.15	0.943

Ti not included.
[a]Late berthierine (for comparison).
ΣMe = cation sum; ^{IV}Al = on the basis of $^{IV}Al + ^{IV}Si = 4$; Fe rat. = Fe:(Fe + Mg) ratio; Vac. = vacancy.
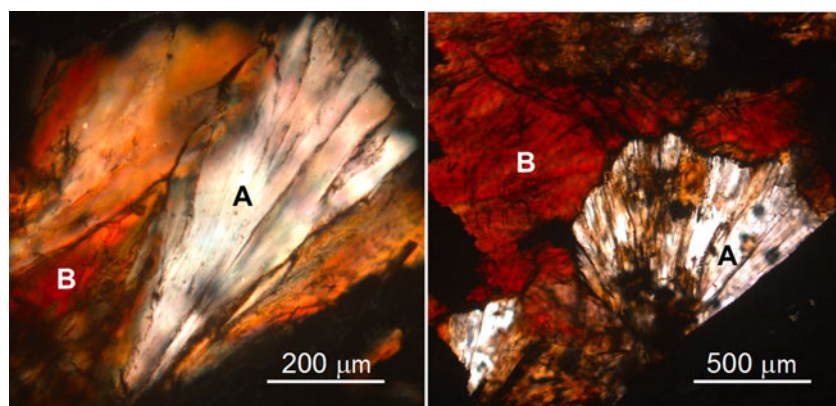
Fig. 2. Two examples of pleochroism of red chamosite (thin section, uncrossed polars). White elongated areas (A type): polar sub-perpendicular to (001); dark orange-red areas (B type): polar sub-parallel to (001). Dark zones: pyrite.

~895 and ~1110 nm, with a weak band on its left flank at ~710 nm. At <650 nm, a broad ($\Delta\nu_{1/2} \approx 3700$ cm^{-1}; graphic estimation) and strong absorption band centred at ~550 nm (~18 200 cm^{-1}) superimposed on the sloping continuum is observed, causing the absorption of the green colour. This corresponds to the loss of transmittance observed in spectrum B of Fig. 3.

2. Region II (from 1350 to 2500 nm) is very similar in terms of the A and B spectra. It shows weaker absorption bands, dominated by vibrational transitions, with two sub-regions:

   i. A small sharp band at 1415 nm, followed by three ill-defined broad bands at 1580, 1720 and ~1770 nm.

   ii. At wavelengths over 1850 nm, a complex band composed of (at least) three distinct bands at ~2268, 2320 and 2370 nm, preceded by two small bands at ~2020 and 2180 nm.

Discussion

Geochemical evolution of chamosite at Saint-Aubin-des-Châteaux

According to the paragenetic sequence (Table 1) and EPMA data (Fig. 1a), the smallest values of ^{IV}Al correspond to chamosite associated with quartz, such as in sandstone (No. 15 and No. 16) or in lulzacite-bearing veinlets (No. 13). Conversely, ^{IV}Al-rich chamosite (green and red, analyses No. 2–11) is related to the beginning of the hydrothermal process (stages 1 and 2), with a strong contribution of the hydrothermal fluids, which would indicate the greatest leaching of SiO_2 relative to Al_2O_3. In addition, the calculated structural formulae are closer to stoichiometric $(Fe_4Al_2)(Si_2Al_2)O_{10}(OH)_8$ than to the classic chamosite structural formula $(Fe_5Al)(Si_3Al)O_{10}(OH)_8$, with the Al-poorest compositions (analyses No. 14–16; Table 3) close to the middle of the solid solution (*i.e.* approximately $(Fe_{4.5}Al_{1.5})(Si_{2.5}Al_{1.5})O_{10}(OH)_8$. The average composition of red chamosite has Fe:(Fe + Mg) = 0.943 (±0.013) and ^{IV}Al = 1.673 (±0.035).

The first chamosite sample from Saint-Aubin analysed by Chauvel (1971) was extracted from the primitive oolitic ore. The analysis yielded a similar Fe:(Fe + Mg) ratio (0.946), but a lower Al content (^{IV}Al = 1.33). Such an Al deficit may be due to minor quartz admixture in the sample selected for wet chemical analysis.

The variation of vanadium content is related to the evolution of the ore deposit established by Gloaguen *et al.* (2007):

1. Primitive green chamosite has a low V_2O_3 content (0.25 wt.% – analysis No. 1; Tables 2 & 3). Chamosite from the oolitic–chloritic facies (analysis No. 3), with only 0.10 wt.% V_2O_3,
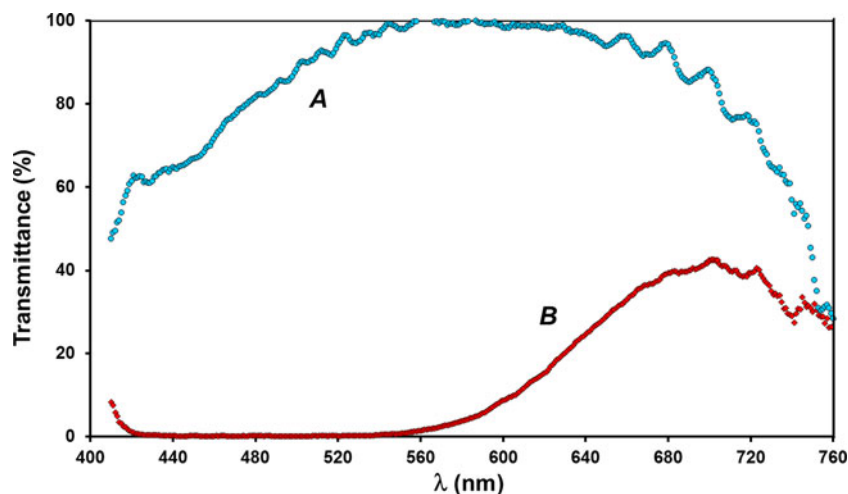
Fig. 3. Visible transmittance spectra of red chamosite using a polarizing microscope (thin section). A spectrum (blue-spot curve): **E** ⊥ (001), white; B spectrum (red-spot curve): **E** ∥ (001), dominantly red.
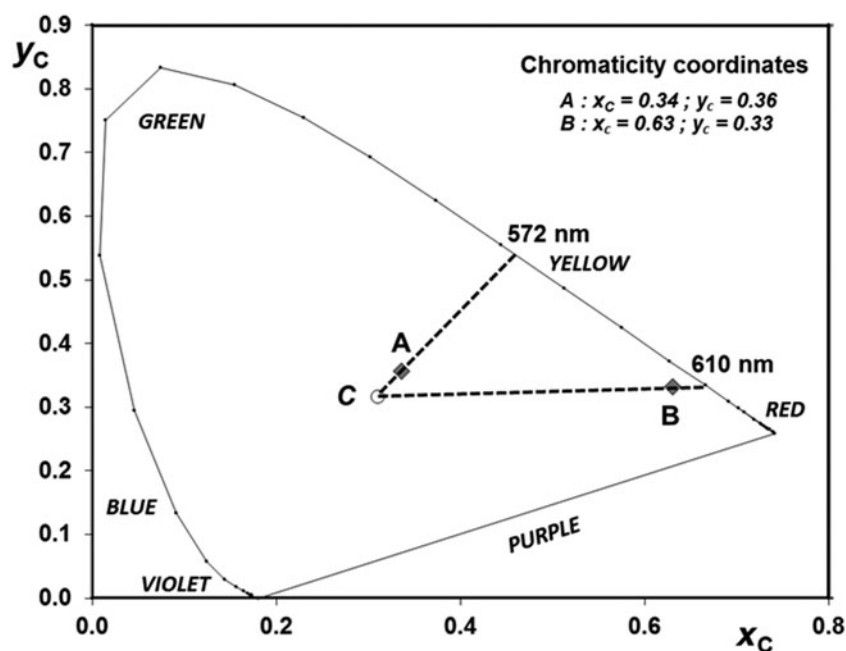

Fig. 4. Representation of pleochroism colours of red chamosite in the CIE chromaticity diagram. C = white colour ('average daylight' illuminant). Horseshoe-shaped line: spectrum locus (pure colours of the visible spectrum). Segment from violet to red: line of purple colours. A: **E** ⊥ (001); B: **E** ∥ (001).

apparently corresponds to residual primary chamosite, after dissolution of the siderite matrix of the oolitic iron ore at the beginning of stage 1.

2. The V content increases significantly in green or red chamosite crystallized during stages 1 and 2, up to 1.06 wt.% V_2O_3. In sample 11 (red chamosite), crystal zoning indicates a V decrease from the centre to the rim (1.06–0.58 wt.% V_2O_3).

3. Then, in stages 2 and 3, the V content decreases. In sulfide veins within the hydrothermalized ironstone (stage 2), the V content is only 0.24 wt.% V_2O_3. In final generations (*i.e.* in lulzacite-bearing quartz–siderite veinlets within the ironstone (stage 2) or in sulfide or sulfosalt quartz veins within surrounding sandstone (stages 2 and 3), the V content decreases to very low concentrations (≤0.03 wt.% V_2O_3). This decrease indicates leaching of vanadium by late hydrothermal solutions.

There is no significant variation of the TiO_2 content, which is always very small (0.01–0.03 wt.%; Tables 2 & 3). Similarly, the MnO content is small (0.0–0.3 wt.%), with a small enrichment in green chamosite of stage 3 (up to 0.29 wt.%), while in red chamosite it does not exceed 0.12 wt.%.

Position of chamosite varieties from Saint-Aubin in the chamosite–clinochlore series

The chamosite composition field from Saint-Aubin agrees with the general trend of an increase of $^{IV}Al^{3+}$ with increasing Fe:(Fe + Mg) ratio (Brown & Bailey, 1962; Hillier & Velde, 1991). On the basis of an extended chemical database on metamorphic chlorite, Zane *et al.* (1998) established a regression line between the clinochlore and chamosite poles, from Mg = 4.81 to Fe = 4.38 atoms; that is, if there are no vacancies, ^{IV}Al varies from 1.19 up to 1.62 (Fig. 6a). Figure 6a also shows the composition field of the main polytype II*b* determined by Brown & Bailey (1962) on the basis of XRD data. In Saint-Aubin, chamosite analyses fill the gap between the II*b* field and the solid solution of pure chamosite
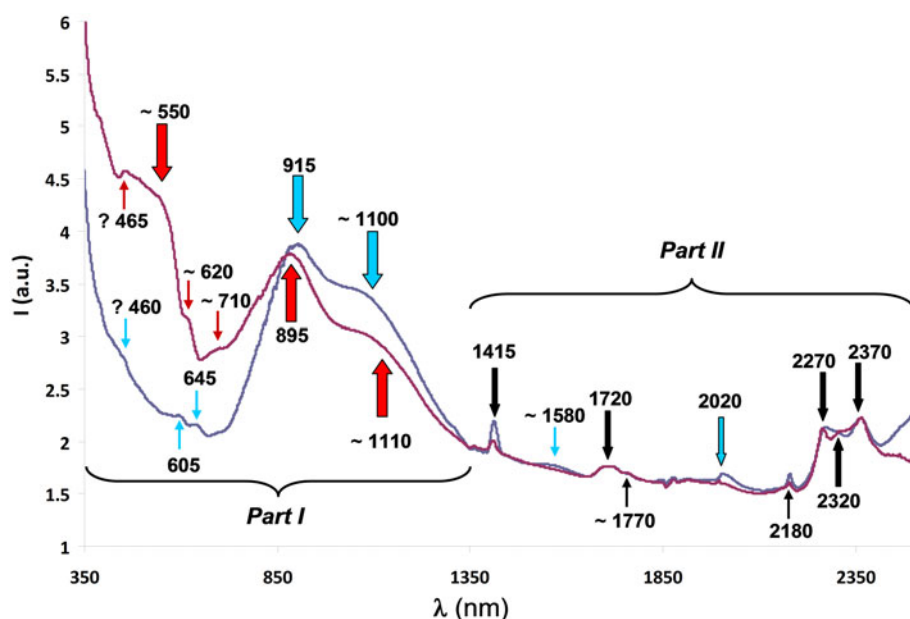
Fig. 5. Vis–NIR absorption spectrum of red chamosite (thin section, transmitted light). Blue line: **E** ⊥ (001); red line: **E** ∥ (001). Blue and red arrows refer to specific band characteristics of the blue and red spectra, respectively; black arrows in part II indicate common absorption bands. a.u. = absorbance unit.

Table 4. Absorption bands in the Vis–NIR absorbance spectra of red chamosite.

λ (nm)	ν (cm^{-1})	I	W	A	B
460?	21 740	vw	?		
465?	21 705	vw	f		X
~550	18 180	m	L		X
605	16 530	vw	f	X	
~620	16 130	vw	f		X
645	15 505	vw	f	X	
~710	14 085	vw	m		X
895	11 175	VS	L		X
915	10 930	VS	L	X	
~1100	9090	S	L	X	
~1110	9010	S	L		X
1415	7070	w	f	X	X
		vw	f		
~1580	6330	vw	m	X	
1720	5815	w	m	X	X
~1770	5650	vw	f	X	X
2020	4950	w	m	X	
2180	4585	w	f	X	X
2270	4405	m	f	X	X
2320	4310	w	f	X	X
2370	4220	m	m	X	X

A = **E** ⊥ (001); B = **E** ∥ (001).
Intensity scale (I): VS = very strong; S = strong; m = medium; w = weak; vw = very weak; ? = doubtful.
Width scale (W): L = large; m = medium; f = fine.

IIb determined experimentally by Parra *et al.* (2005) in the 350–530°C range, with $1.2 < {}^{IV}Al < 1.8$ atoms per $O_{10}(OH)_8$. In addition, Fig. 6a shows the compositions of chlorite samples with well-resolved crystal structures (Table 5). Ordered triclinic clinochlore studied by Smyth *et al.* (1997), with ${}^{IV}Al = 1.04$ and Fe:(Fe + Mg) = 0.02, can be taken as the reference for the Mg end-member. Only one crystal structure of chamosite IIb (Mg-rich) is known: that of Walker & Bish (1992), with Fe:(Fe + Mg) ≈ 0.6 and ${}^{IV}Al = 1.15$. To date, there are no crystal structure data for Mg-poor or Mg-free chamosites of the most common IIb polytype.

McOnie *et al.* (1975) have established the variation of the unit cell in synthetic chlorites of the clinochlore–'daphnite' solid solution ('daphnite' = chamosite). The regular increase of the unit volume *V* with increasing ${}^{VI}Fe^{2+}$ gives $V \approx 712$ Å^3 for the Fe endmember. According to Tschermak substitution, Parra *et al.* (2005) give *V* between 711 and 719 Å^3. On the basis of Fe:(Fe + Mg) = 0.94, the unit cell of red chamosite would be $a = 5.393$ Å, $b = 9.356$ Å, $c = 14.212$ Å, β = 97.2° and $V = 711.4$ Å^3 (McOnie *et al.*, 1975). The lower values of the measured *a*, *b* and *c* parameters of red chamosite (5.375, 9.322 and 14.177 Å, respectively) relative to these calculated values are artefacts related to the single-crystal XRD approach. Disorder stacking in clay minerals induces a distortion of the profile of diffraction peaks towards higher 2θ values (*i.e.* lower interplanar distances) (Brindley, 1980). Hence, the mean positions of diffraction spots recorded through single-crystal XRD analysis will give lower values of unit-cell parameters. Moreover, interstratification with berthierine cannot be excluded, as it would not change significantly the chemical composition or the dimensions of the 7 Å sub-unit cell (Inoué & Kogure, 2016).

Comparison with other Mg-poor chamosite occurrences

Various occurrences of Mg-poor chamosite have been described in the past. Table 6 lists their structural formulae. Chamosite is a common component of oolitic ironstones, such as in central Brittany (Chauvel, 1971), in Switzerland (Delaloye & Odin, 1988) or in the Iberian Massif (Zamora, Spain; Fernández & Moro, 1996). All are Al-rich (${}^{IV}Al$ >1.3 atoms per 4 tetrahedral sites) and Mg-poor (Fe:(Fe + Mg) >0.85) (Fig. 6b). One exception would be that of chamosite from the type deposit of Chamoson (Switzerland; analysis not shown). The wet analysis of the latter chamosite (Delaloye & Odin, 1988) indicates a very low ${}^{IV}Al$ (~0.88), together with a Si excess, probably due to quartz impurities. Unfortunately, there is a lack of EPMA results. 'Bavalite' from the Devonian stratiform iron ore of Bas-Vallon (central Brittany; Orcel, 1923) is a chamosite that is close to that of Saint-Aubin, with ${}^{IV}Al ≈ 1.46$ and Fe:(Fe + Mg) = 0.91. Saint-Aubin chamosite represents the ${}^{IV}Al$-richest and Mg-poorest compositions among the oolitic ores. In the Kidd
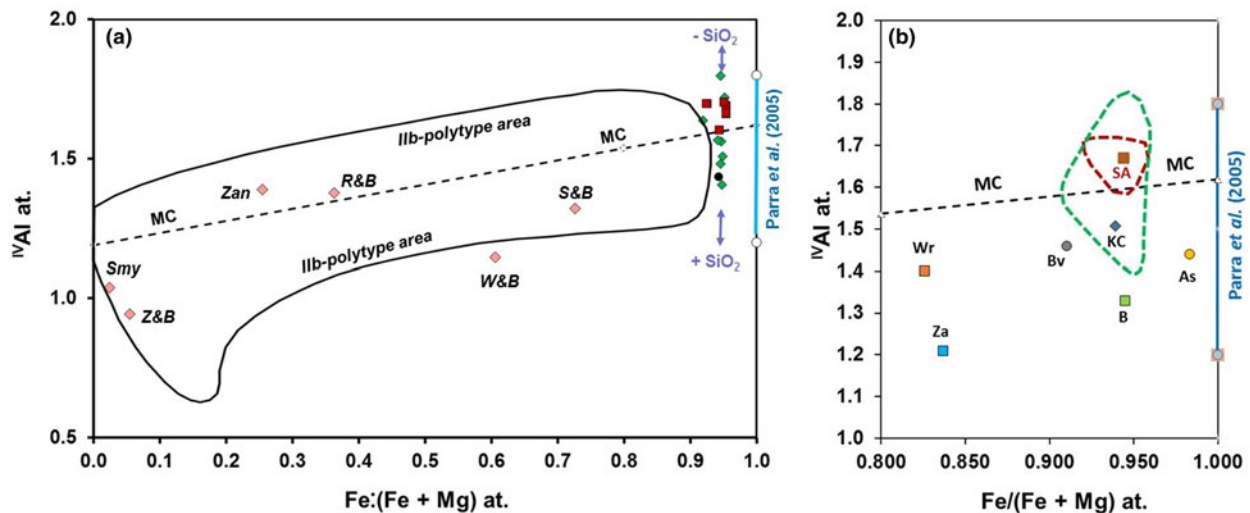
Fig. 6. Comparison of chamosite from Saint-Aubin with a sequence of chlorites from clinochlore to chamosite. (a) Representation of chamosite analyses from Saint-Aubin in the clinochlore–chamosite series (green diamonds: green variety; red squares: red variety). Black circle: berthierine. Large composition field: area of II*b* polytype of Brown & Bailey (1962). Dotted line (MC): regression line for metamorphic chlorite (Zane *et al.*, 1998). Pink diamonds: Compositions from crystal structures (see Table 5). Blue segment: Tschermak substitution range in synthetic pure chamosite (Parra *et al.*, 2005). (b) Detail in the Fe-rich part of the series. Green and red dashed lines: composition fields of green and red chamosite varieties from Saint-Aubin, respectively. SA: mean composition of red chamosite. Wr, Za, Bv and B: chamosite from oolitic ironstones; KC and As: chamosite from sulfide deposits.
As = Ashio; B = Brittany; Bv = Bas Vallon; KC = Kidd Creek; SA = Saint-Aubin; Wr = World; Za = Zamora; R&B = Rule & Bailey (1987); S&B = Shirozu & Bailey (1965); Smy = Smyth *et al.* (1997); W&B = Walker & Bish (1992); Z&B = Zheng & Bailey (1989); Zan = Zanazzi *et al.* (2006).

Table 5. Selected crystallographic parameters and chemical compositions of members of the clinochlore–chamosite series with well-known crystal structures.

Species	Structural formula	Polytype	β (°)	V (Å³)	Fe ratio	^{IV}Al	Ref.
Chamosite	$(Fe_{3.42}Mg_{1.29}Al_{1.29})(Si_{2.68}Al_{1.32})O_{10}(OH)_8$	I*b*	90.01	712.85	0.726	1.32	Shirozu & Bailey (1965)
Chamosite	$(Fe_{2.72}Mg_{1.77}Al_{1.33}Mn_{0.08}\square_{0.1})(Si_{2.85}Al_{1.145}Ti_{0.005})O_{10}(OH)_8$	II*b*	97.23	706.74	0.606	1.145	Walker & Bish (1992)
Clinochlore	$(Fe_{1.69}Mg_{2.96}Al_{1.275})(Si_{2.624}Al_{1.376})O_{10}(OH)_8$	II*b*	96.35	703.14	0.363	1.376	Rule & Bailey (1987)
Clinochlore	$(Fe_{1.88}Mg_{5.53})(Si_{2.61}Al_{1.39})O_{10}(O\ H)_8$	II*b*	97.2	701.74	0.254	1.39	Zanazzi *et al.* (2006)
Clinochlore	$(Fe_{0.269}Mg_{4.715}Al_{0.694}Fe_{0.109}Cr_{0.128}Ni_{0.011})(Si_{3.056}Al_{0.944})O_{10}(OH)_8$	II*b*	96.82	701.19	0.054	1.944	Zheng & Bailey (1989)
Clinochlore	$(Fe_{0.118}Mg_{4.882}Al_{0.841}Fe_{0.102}Cr_{0.004}Ti_{0.004}\square_{0.049})(Si_{2.96}Al_{1.04})O_{10}(OH)_8$	II*b*	97.47	698.35	0.024	1.04	Smyth *et al.* (1997)

Fe ratio = Fe^{2+}:(Fe^{2+} + Mg).

Table 6. Structural formulae per $O_{10}(OH)_8$ of natural Mg-poor chamosites (Fe:(Fe + Mg) >0.80).

Formula ($O_{10}(OH)_8$ omitted)	^{IV}Al	Fe:(Fe + Mg)	Deposit	Ref.
$(Fe_{3.87}Mg_{0.23}Mn_{0.01}\square_{0.07}Al_{1.74}V_{0.07})(Si_{2.33}Al_{1.67})^a$	1.67	0.944	Saint-Aubin	This study
$(Fe^{2+}_{4.14}Fe^{3+}_{0.07}Mg_{0.40}Al_{1.39})(Si_{2.50}Al_{1.50})^b$	1.50	0.912	Bas Vallon	Orcel (1923)
$(Fe_{4.12}Mg_{0.07}Mn_{0.01}\square_{0.11}Al_{1.69})(Si_{2.56}Al_{1.44})$	1.44	0.983	Ashio	Inoué & Kogure (2016)
$(Fe^{2+}_{4.21}Fe^{3+}_{0.05}Mg_{0.27}Mn_{0.01}Al_{1.46})(Si_{2.49}Al_{1.51})$	1.51	0.940	Kidd Creek (average)	Jiang *et al.* (1992)
$(Fe^{2+}_{4.11}Fe^{3+}_{0.05}Mg_{0.07}Mn_{0.01}Al_{1.48})(Si_{2.48}Al_{1.52})$	1.52	0.983		
$(Fe^{2+}_{4.25}Mg_{0.07}Mn_{0.06}Al_{1.50})(Si_{2.50}Al_{1.50})$	1.50	0.986		
$(Fe_{3.75}Mg_{0.73}Mn_{0.04}\square_{0.06}Al_{1.42})(Si_{2.79}Al_{1.21})$	1.21	0.837	Zamora	Fernandez *et al.* (1998) (mean of 7 analyses)
$(Fe_{3.44}Mg_{0.20}\square_{0.6}Al_{1.42})(Si_{2.70}Al_{1.30})$	1.33	0.945	Brittany	Chauvel (1971)
$(Fe_{3.80}Mg_{0.80}Al_{1.40})(Si_{2.60}Al_{1.40})^c$	1.40	0.826	World	Chauvel (1990), in Fernandez *et al.* (1998)

[a] Red chamosite (mean).
[b] 'Bavalite' (wet analysis).
[c] World ironstones (mean of 50 analyses).

Creek massive sulfide deposit (Ontario), the Mg-poorest chamosite analyses (Jiang, 1992) plot within the field of chamosite from Saint-Aubin (Fig. 6b). A very Mg-poor chamosite ($^{IV}Al \approx 1.44$, Fe:(Fe + Mg) = 0.983; Fig. 6b) has been found in the Ashio polymetallic vein deposit (Japan; Inoué & Kogure, 2016).

All of these chamosite analyses are close to the solid-solution field of synthetic Mg-free chamosite of Parra *et al.* (2005). Clearly,

all of these data on natural Mg-poor as well as synthetic Mg-free chamosites contain more Al than the stoichiometric formula $(Fe_5Al)(Si_3Al)O_{10}(OH)_8$ given by Bayliss (1975) for the definition of this chlorite species. On the other hand, they contain Al below the stoichiometric formula $(Fe_4Al_2)(Si_2Al_2)O_{10}(OH)_8$. In a temperature range corresponding to metamorphic as well as high-temperature hydrothermal conditions, the ideal composition

field (without vacancies) of Mg-free chamosite is restricted to a solid solution between $(Fe_{4.8}Al_{1.2})(Si_{2.8}Al_{1.2})O_{10}(OH)_8$ and $(Fe_{4.2}Al_{1.8})(Si_{2.2}Al_{1.8})O_{10}(OH)_8$ (Para *et al.*, 2005). Thus, chemical analyses on natural as well as synthetic samples show that chamosite is definitively a non-stoichiometric mineral species. It corresponds to the general formula $(Fe_{5-x}Al_{1+x})(Si_{3-x}Al_{1+x})O_{10}(OH)_8$, with $0.2 < x < 0.8$.

Interpretation of Vis–NIR spectra of red chamosite

The Vis–NIR spectra A and B (Fig. 5) were compared with published spectra of members of the clinochlore–chamosite series. Faye (1968) reported absorption bands of oriented lamellae of green chlorite with 5.2 wt.% Fe^{2+} and 0.6 wt.% Fe^{3+} in the range 8000–29,000 cm^{-1} (1250–345 nm). For a transverse section, there are two bands at low energy (11,600 and 9600 cm^{-1}), while for a basal section, together with the same bands at 11,400 and ~9500 cm^{-1}, an additional feature is present at 14,100 cm^{-1}. Platonov (1976) also described three bands in the unpolarized absorbance spectrum of chamosite at 14,300, 11 350 and 9200 cm^{-1}.

In the clinochlore–chamosite series, the two components at ~11,500 and 9500 cm^{-1} correspond to electronic transitions of octahedral Fe^{2+}, while the third at ~14,300 cm^{-1} represents an intervalence charge transfer (IVCT) between Fe^{2+} and Fe^{3+} in adjacent M_1 and M_2 octahedra (Platonov, 1976). This third component is absent in spectrum A and weak in spectrum B (~710 nm/14,085 cm^{-1}), indicating a very low Fe^{3+} content in red chamosite from Saint-Aubin. It would be interesting to quantify such a weak Fe^{3+} content of red chamosite through X-ray absorption near-edge structure measurement at the microscopic scale (Vidal *et al.*, 2006; Trincal *et al.*, 2015). The weak band at ~620 nm (Fig. 5) may correspond to the large absorption band at 609 nm observed in a green V-rich, Fe-free muscovite, which corresponds to a V^{3+} electronic transition (Ertl *et al.*, 2019).

At >1350 nm (Part II of the A and B spectra in Fig. 5), absorption bands correspond to the overtones and combinations of the fundamental OH and H–O–H vibrations. At the shortest wavelengths, the A and B spectra can be compared with the NIR spectrum obtained for clinochlore between 1350 and 1670 nm (Ferrage *et al.*, 2003): two close sharp bands at 1392 (main) and 1405 nm and two broad ones near 1440 and 1560 nm. The first sharp band, corresponding to the OH-stretching mode of Mg_3OH, is not visible in red chamosite due to its low Mg content. The second band was tentatively assigned by Ferrage *et al.* (2003) to an OH-stretching mode of Mg_2AlOH. They relate the two other broad bands (1440 and 1560 nm) to overtones of OH-stretching fundamental modes of (SiSi)O–OH and (SiAl)O–OH, respectively. The band of the first mode is not visible in the Saint-Aubin sample, as would be expected from its low Si content.

Bishop *et al.* (2008) acquired NIR reflectance spectra of clinochlore and chamosite and reported three bands at ~1400 (sharp), 1450 (broad) and 1550 nm (broad), and two broad bands at 1880 and 2000 nm in clinochlore. All of these bands are very weak (1400, 1890 and 2010 nm) or lacking in chamosite. Mathian *et al.* (2018) observed a doublet at 1391 and 1406 nm for clinochlore and at 1407 and 1415 nm for chamosite, in accordance with Ferrage *et al.* (2003).

In the region of highest wavelengths (>2200 nm), Bishop *et al.* (2008) described the triplet 2250/2290/2330 nm for clinochlore, or 2260/2310/2360 nm for chamosite. Recently, Mathian *et al.*

(2018) indicated four bands in clinochlore (2247, 2296, 2326 and 2393 nm) and only two in chamosite (2259 and 2351 nm), with a third one (weak, not measured) between these two bands. In our sample, the two main bands of this complex absorption band centred at ~2300 nm show a shift towards higher wavelengths from clinochlore to chamosite, with the highest values measured for red chamosite (2270 and 2370 nm).

Relative to the general characteristics of the visible spectra of the members of the clinochlore–chamosite series, that of red chamosite presents two peculiarities: a weak Fe^{3+} absorption band indicative of the very low content of this ion and the presence of a broad band centred at ~550 nm. Alone, this last band would induce a pink to purple colour. Combined with the underlying continuum rising towards the UV, it is responsible for the orange-red colour of this chamosite variety. From Fig. 5, the absorption coefficient of the 550 nm band can be estimated to be ~1 absorbance unit for a thickness of 30 µm, leading to an approximate value of 30 A mm^{-1}, which is considerable. This means that the absorber is very efficient.

Origin of the colour of red chamosite

The colour of minerals is a complex problem that is controlled by various physical-chemical factors (Fritsch & Rossman, 1987, 1988). Many coloured varieties of nominally colourless minerals are related to the presence of a small number of elements, often from the first series of transition metals. They may absorb in the visible range due to electronic transitions within their orbitals (d–d, or crystal field transitions) or due to electronic transitions between two atoms, called IVCT transitions. Finally, in some cases, absorption is due to colour centres, often linked to natural radiation damage. Other causes of colour in minerals are not directly related to absorption and are thus irrelevant to this discussion. The key facts for the interpretation of the visible absorption data are that the colour-causing band centred at ~550 nm is quite wide ($\Delta\nu_{1/2} \approx 3700$ cm^{-1}), very strongly absorbing (~30 A mm^{-1}) and very strongly pleochroic (near-white or near-colourless to a dark colour). In addition, it appears to be linked to vanadium.

In the following discussion, one must bear in mind that the hydrothermal process that produced red chamosite is governed by a redox mechanism. This would allow for a greater oxidation state among cations of the transition elements present in red chamosite.

Role of vanadium enrichment

The EPMA results clearly indicate that red chamosite displays V enrichment relative to primitive chamosite, while there is no positive correlation with Mn and Ti contents, which are always very low. Such a V enrichment may be explained without an external source if one considers that the volume of neoformed chamosite is minor relative to that of dissolved primitive chamosite: as the main part of iron from this primitive chamosite re-precipitates as pyrite, there will be a relative residual V enrichment, which leads to an increase in the V:Fe ratio of neoformed chamosite (Gloaguen *et al.*, 2007).

Tables 2 & 3 show that the V content of hydrothermal green chamosite may be as high as that of the red variety (compare No. 5 and No. 6 of Table 2). Thus, the presence of V in chamosite appears to be a necessary but not sufficient condition for the formation of the red variety. This is confirmed by Whitney &

Northrop ([1986](#)), who have described a V-rich chlorite of (normal) green colour, where V (mainly trivalent) is concentrated in the octahedral sites of the brucite-type sheet. In similar samples, Meunier ([1994](#)) considers only V^{3+}, which substitutes Al in octahedral sheets.

A mineral similar to red chlorite in an intimate intergrowth of chlorite with biotite or hematite has been described in a transmission electron microscopy study (Mellini *et al.*, [1991](#)). Here, the red colour is mainly due to the Fe^{3+} of hematite, which shows two absorption bands at 12,000 and 16,000 cm^{-1} (Platonov, [1976](#)) and is lacking in red chamosite.

Oxidation state of vanadium

In Saint-Aubin, the dispersion of red chamosite within the oolitic ore and its low V content has precluded up to now the characterization of V oxidation state(s) through analytical methods. Oxidation states 2+ and 5+ can be excluded for V because V^{2+} prevails only in strongly reducing conditions (below the iron/wüstite buffer), while V^{5+} implies a high f_{O_2} (Papike *et al.*, [2016](#)). In aqueous systems (normal conditions; pH neutral to acid) and at low Eh, V^{3+} (solid or aqueous species) is the stable oxidation state (Takeno, [2005](#); Povar *et al.*, [2019](#)), which coexists with Fe^{2+}. V^{4+} species appear at higher Eh, always in the stability field of Fe^{2+} (Takeno, [2005](#)). According to Takeno ([2005](#)), in the same conditions, Mn^{2+} is the only stable oxidation state of Mn. Mn^{3+} appears at basic pH and Mn^{4+} at high Eh.

In Saint-Aubin, abundant organic matter will favour V^{3+} in chamosite, as in vanadium mica roscoelite, $KV_2AlSi_3O_{10}(OH)_2$. In red chamosite, the weak band at 620 nm has been tentatively related to V^{3+}. The oxidation process related to hydrothermal stages may also have stabilized V, at least partly, to the V^{4+} state.

In similar geological environments with reducing conditions (graphite-bearing metamorphic series), only V^{3+} and V^{4+} have been detected, such as in tanzanite, a V-bearing variety of zoisite, $Ca_2Al_3(Si_2O_7)(SiO_4)O(OH)$, from Merelani, northeast Tanzania (Olivier, [2006](#)), as well as in the V-rich oxide minerals of the Green Giant vanadium–graphite deposit, southwest Madagascar (Di Cecco *et al.*, [2018](#)). In the Kola region (Russia), various V minerals contain exclusively V^{3+} (Kompanchenko *et al.*, [2018](#)). If the colour is linked to V, then it may be compared to that of various V compounds.

Colour of vanadium oxides and silicates

Evans & White ([1987](#)) reviewed the colour of V minerals. In V oxides, without the influence of other transition metals, which may induce crystal field or IVCT transitions, the colour is controlled by the oxidation state of V. With V^{5+} (no 4s or 3d valence electrons), minerals are uncoloured or weakly absorbent. Oxides and hydrates of V^{4+} are green (*i.e.* haradaite, $Sr(VO)(SiO_3)_2$) or blue (*i.e.* pentagonite, $Ca(VO)(Si_4O_{10}).4H_2O$); V^{3+} oxides and silicates are black (*e.g.* karelianite, V_2O_3) or strongly absorbent. The Fe-free roscoelite $K(V^{3+},Al)_2(AlSi_3O_{10})(OH)_2$, a muscovite isotype, is green (Ito, [1965](#)).

When substituting as traces or minor components in oxides, V^{4+} gives a green colour, as in malayaite ($CaSnSiO_5$), where V^{4+} replaces Sn^{4+} (Joo & Lee, [2010](#)). V^{3+} also gives a green colour in beryl (V-rich emerald), as well as in muscovite (Uher *et al.*, [2008](#); Ertl *et al.*, [2019](#)) and in a number of other minerals and gems (Fritsch & Rossman, [1987](#)).

In the general review of the colours of minerals by Platonov ([1976](#)), only blue to violet tanzanite (Faye & Nickel, [1971](#)) shows an absorption band ($\sim$555 nm) close to but distinct from the specific band of red chamosite at 550 nm ([Fig. 5](#)). In all of the studies we reviewed, there is not a single example of a V mineral with a red colour strictly due to V. Thus, the possibility of the 550 nm band originating from isolated V^{3+} or V^{4+} is negligible.

Role of other elements

Other isolated transition metal ions can be eliminated as well. In general, transition metal ions produce less absorbing, less pleochroic and narrower bands. The absorption of Fe ions has been discussed earlier, and they do not have a band at 550 nm. Of the remaining transition metals, only Mn and Ti are present in detectable amounts. Mn, although a common colouring agent in minerals, can be ruled out: as Mn^{2+}, it is so weakly absorbing that it has to be present at several wt.% element concentration units (typical of nominal Mn minerals) to give a pink to red colour. However, the concentration of Mn is quite small in Saint-Aubin chamosite. In addition, in the conditions prevailing at Saint-Aubin, Mn^{2+} is the only stable oxidation state of Mn (Takeno, [2005](#)). Thus, we do not expect to detect the absorption of Mn^{3+}, although it is a far more efficient absorber, but this valence is the result of either natural irradiation (and there are no traces of irradiation in the Saint-Aubin minerals) or of basic pH (Takeno, [2005](#)), which do not correspond to the environment characterized for red chamosite. Similarly, for Ti, efficient colouration in minerals is obtained only through Ti^{3+}, which is also a product of natural irradiation, absent here, or very reducing conditions (such as meteorites), which do not correspond to the redox conditions at the time of deposition. Therefore, isolated metal ions can be eliminated as the potential cause of the red colour in our chamosite.

Colour centres rarely absorb as strongly as the 550 nm band. They may be strongly pleochroic, such as when the colour centre itself is a planar molecular ion (such as CO_3^- in beryl; Fritsch & Rossman, [1988](#)). Thus, combined again with the absence of irradiation, colour centres are very unlikely causes of this absorption. It follows that only charge-transfer (IVCT) processes offer the observed combination of extremely efficient absorption, very strong pleochroism and rather broad bands (Mattson & Rossman, [1987](#)) required to explain the results of this study.

Charge-transfer mechanism

Examples of IVCT include mostly Fe^{2+}–Fe^{3+} in a variety of minerals, such as beryl, cordierite and lazulite (Fritsch & Rossman, [1988](#)). Furthermore, here, the pleochroism is particularly intense, going from near colourless to a very dark colour, as is the case for many charge-transfer processes (as in the three examples cited before). Thus, the exceptionally strong pleochroism combined with the exceptionally large absorption coefficient strongly support the IVCT working hypothesis, which is the only type of absorption mechanism to which these two properties are typically associated.
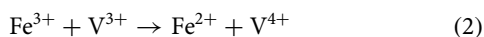
The large width of the 550 nm absorption band ([Fig. 5](#)) is an additional argument for IVCT. Even though the value of $\Delta\nu_{1/2}$ ($\sim$3700 cm^{-1}) may appear low relative to the common interval of 5000–6300 cm^{-1} for Fe^{2+}/Fe^{3+} IVCT (Mattson & Rossman, [1987](#)), it is in accordance with the lowest values of 3150 and 3575 cm^{-1} indicated by these authors for biotite and chlorite, respectively.

According to the EPMA results and the spectroscopic study, only the Fe/V pair can be considered for such an IVCT ‖ (001). A heteronuclear charge transfer between two cations M_1 and M_2
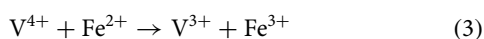
in adjacent octahedra, with oxidation states $m+$ and $n+$, respectively, corresponds to the general formula in Eq. (1):

$$M_1^{m+} + M_2^{n+} \rightarrow M_1^{(m-1)+} + M_2^{(n+1)+} \qquad (1)$$
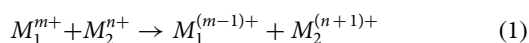
In addition, Fe^{3+} is minor relative to Fe^{2+}, as indicated by the weak absorption band at 710 nm in the Vis–NIR spectra (Fig. 5), which would correspond to Fe^{2+}/Fe^{3+} IVCT. Two solutions are possible for Eq. (1):

$$Fe^{3+} + V^{3+} \rightarrow Fe^{2+} + V^{4+} \qquad (2)$$

or conversely:

$$V^{4+} + Fe^{2+} \rightarrow V^{3+} + Fe^{3+} \qquad (3)$$

The IVCT according to Eq. (2), which implies the presence of Fe^{3+} and V^{3+} in adjacent octahedra and both of low concentration in chamosite, is less probable than the IVCT in Eq. (3), as there will always be an Fe^{2+} ion adjacent to any V-containing octahedron. Hence, the IVCT in Eq. (3) appears to be the best proposal to explain the broad absorption band at ∼550 nm.

No IVCT such as that in Eq. (3) has been documented previously. It would be similar to the Fe^{2+}/Ti^{4+} IVCT described in dumortierite and other (Fe, Ti)-bearing silicates (Platonov *et al.*, 2000, and references herein). Nevertheless, in the case of dumortierite, Fe and Ti are in face-sharing octahedra with a short Fe–Ti distance and with direct overlapping of the T_{2g} levels. In edge-sharing octahedra, there must be an indirect charge transfer via bridging oxygen.

Resulting colour

When reconsidering spectroscopic data in the visible range according to IVCT mechanism, the red colour of chamosite is the sum of two opposite spectroscopic characteristics: (1) an absorption band due to Fe/V IVCT, which absorbs the green colour owing to minor V; and (2) a good transparency in the orange-red part of the spectrum due to very low Fe^{3+}. This transparency is a rather special characteristic because, generally, chlorite has a significant Fe^{3+} content that would induce an absorption band at ∼700 nm (Fe^{2+}/Fe^{3+} IVCT).

Oxidation conditions

In Saint-Aubin, the sulfidation of the oolitic iron ore is the result of a geochemical process combining siderite leaching and redox reactions between organic matter and the hydrothermal solution (Gloaguen *et al.*, 2007). The organic matter acted as a buffer to control the strong reducing conditions as long as it was in close contact with the hydrothermal solution and allowed the crystallization of green chamosite. Conversely, when this buffer was not operating locally, the hydrothermal solution induced a weak increase of f_{O_2} and the crystallization of red chamosite.

Formation of red chamosite would be the result of the strongest interaction of the oxidant hydrothermal solution with primitive oolitic ore, according to the preferred location of red chlorite in the strongest reaction zones (alteration haloes) between massive sulfide lenses and oolitic ironstone. Around these zones, chamosite may have crystallized at the same time with similar V contents, but with a normal green colour. The formation of brown

berthierine would indicate a similar increase of f_{O_2} during the late, low-temperature hydrothermal stage.

Summary and conclusions

In Saint-Aubin-des-Châteaux, the interaction between the primitive lower Ordovician oolitic iron ore and an early Variscan hydrothermal solution leads to a complex paragenetic sequence, illustrated by the chemical evolution of chamosite. Together with its ^{IV}Al content, the V concentration is the best marker of this evolution, with its highest values related to the maximal hydrothermal remobilization of the oolitic ore at the beginning of the process. This leads to the formation of a red variety of chamosite, related to a local increase of f_{O_2} when the primitive organic matter did not act locally as a buffer of reducing conditions.

As a whole, the chamosite composition field from Saint-Aubin fills the gap between the solid-solution field of the II*b* polytype in natural compounds defined by Brown & Bailey (1962) and synthetic Mg-free chamosite (Parra *et al.*, 2005). While the Fe:(Fe + Mg) ratio is relatively constant, the ^{IV}Al content varies significantly from 1.4 up to 1.8 atoms per four tetrahedra, according to variations in SiO_2 local activity. Red chamosite has an Fe:(Fe + Mg) mean ratio of close to 0.944, and that of ^{IV}Al is close to 1.67.

Taking into account EPMAs of Mg-poor natural as well as Mg-free synthetic samples (Fig. 6), the simplified composition of chamosite (Fe-pure, no vacancies) agrees with the non-stoichiometric formula $(Fe_{5-x}Al_{1+x})(Si_{3-x}Al_{1+x})O_{10}(OH)_8$, with $0.2 < x < 0.8$. The stoichiometric formulas $(Fe_4Al_2)(Si_2Al_2)O_{10}(OH)_8$ and $(Fe_5Al)(Si_3Al)O_{10}(OH)_8$, commonly used as theoretical endmembers (so-called 'Fe-amesite' and 'daphnite', respectively) for thermodynamic calculations (Parra *et al.*, 2005; Bourdelle *et al.*, 2013), are outside this solid solution and are purely theoretical, without natural counterpart.

According to the absorption spectrum in the Vis–NIR range, the colour and exceptionally strong pleochroism of red chamosite are explained by the combination of two factors. First, the proposed IVCT mechanism between V and Fe in the trioctahedral sheet (probably $Fe^{3+}–V^{3+} \rightarrow Fe^{2+}–V^{4+}$ charge transfer) absorbs green. Second, the low Fe^{3+} content precludes significant $^{VI}Fe^{2+}/^{VI}Fe^{3+}$ IVCT and favours red transparency.

In order to check this model of Fe/V IVCT, it would be useful to perform Vis–NIR spectroscopic studies on other vanadiferous green chlorites, such as those from Utah (Whitney & Northrop, 1986). According to the proposed model, such a green colour may be due either to the association of two absorption bands at 550 and 700 nm (Fe^{2+}/V^{4+} and Fe^{2+}/Fe^{3+} IVCT, respectively) or to the lack thereof (only Fe^{2+} and V^{3+}).

The oolitic iron ore deposit of Saint-Aubin-des-Châteaux is an original example of the succession of numerous Mg-poor chamosite generations, from primitive weak metamorphic to several hydrothermal varieties. Crystal chemical changes (^{IV}Al and minor V contents) as well as colour changes of chamosite are controlled by the evolution of the geochemistry of the system (Al:Si ratio, redox conditions and chemical exchanges between primitive oolitic ores and hydrothermal solutions).

careful examination performed by Peter C. Ryan (Middlebury College, VA, USA), Associate Editor Javier Cuadros and an anonymous reviewer greatly improved the quality of the manuscript.

References

Bailey S.W. (1980) Structures of layer silicates. Pp. 1–125 in: *Crystal Structures of Clay Minerals and Their X-Ray Identification* (G.W. Brindley & G. Brown, editors), Monograph **5**, Chapter 1. The Mineralogical Society of Great Britain and Ireland, London, UK.

Bailey S.W. (1988) Chlorite structure and crystal chemistry. Pp. 347–403 in: *Hydrous Phyllosilicates (Exclusive of Mica)* (S.W. Bailey, editor), Reviews in Mineralogy **19**. Mineralogical Society of America, Washington, DC, USA.

Bayliss P. (1975) Nomenclature of the trioctahedral chlorites. *Canadian Mineralogist*, **13**, 178–180.

Bishop J.L., Lane M.D., Dyar M.D. & Brown A.J. (2008) Reflectance and emission spectroscopy study of four groups of phyllosilicates: smectites, kaolinite–serpentines, chlorites and micas. *Clay Minerals*, **43**, 35–54.

Bourdelle F., Parra T., Chopin C. & Beyssac O. (2013) A new chlorite geothermometer for diagenetic to low-grade metamorphic conditions. *Contribution to Mineralogy and Petrology*, **165**, 723–735.

Brindley G.W. (1980) Order-disorder in clay mineral structures. Pp. 125–196 in: *Crystal Structures of Clay Minerals and Their X-Ray Identification* (G.W. Brindley & G. Brown, editors), Monograph **5**, Chapter 2. The Mineralogical Society of Great Britain and Ireland, London, UK.

Brown B.E. & Bailey J.F. (1962) Chorite polytypism: I. Regular and semi-random one-layer structures. *American Mineralogist*, **47**, 819–850.

Capitani G.C., Schingaro E., Lacalamita M., Mesto E. & Scordari F. (2016) Structural anomalies in tobelite-2*M*₂ explained by high resolution and analytical electron microscopy. *Mineralogical Magazine*, **80**, 143–156.

Chauvel J.-J. (1971) Contribution à l'étude des minerais de fer de l'Ordovicien inférieur de Bretagne. *Mémoires de la Société géologique et minéralogique de Bretagne*, **16**, 1–244.

Chauvel J.-J. (1974) Les minerais de fer de l'Ordovicien inférieur du bassin de Bretagne-Anjou, France. *Sedimentology*, **21**, 127–147.

Criddle A.J. (1990) Microscope-photometry, reflectance measurement, and quantitative color. Pp. 135–169 in *Advanced Microscopic Studies of Ore Minerals* (J.L. Jambor & D.J. Vaughan, editors), Short Course Handbook, **17**. Mineralogical Association of Canada, Ottawa, Canada.

Delaloye M.F. & Odin G.S. (1988) Chamosite, the green marine clay from Chamoson; a study of Swiss oolitic ironstones. Pp. 7–28 in: *Green Marine Clays: Oolitic Ironstone Facies, Verdine Facies, Glaucony Facies and Celadonite-Bearing Facies – A Comparative Study* (G. S. Odin, editor). Elsevier, Amsterdam, The Netherlands.

Di Cecco V.E., Tait K.T., Spooner E.T.C. & Scherba C. (2018) The vanadium-bearing oxide minerals of the Green Giant vanadium-graphite deposit, southwest Madagascar. *Canadian Mineralogist*, **56**, 247–257.

Ertl A., Rakovan J., Hugues J.M., Bernhardt H.-J. & Rossman G.R. (2019) Vanadium-rich muscovite from Austria: crystal structure, chemical analysis, and spectroscopic investigations. *Canadian Mineralogist*, **57**, 383–389.

Evans H.T. & White J.S. (1987) The colorful vanadium minerals: a brief review and a new classification. *The Mineralogical Record*, **18**, 333–340.

Faye G.H. (1968) The optical absorption spectra of iron in six-coordinate sites in chlorite, biotite, phlogopite and vivianite. *Canadian Mineralogist*, **9**, 403–425.

Faye G.H. & Nickel E.H. (1971) On the pleochroism of vanadium-bearing zoisite from Tanzania. *Canadian Mineralogist*, **10**, 812–821.

Fernandez A. & Moro M.C. (1996) Chemical aspects of the magnetite and chlorite from Ordovician ironstones of the Zamora province (Spain). *Geogaceta*, **20**, 1531–1534.

Fernandez A., Chauvel J.-J. & Moro M.C. (1998) Comparative study of the Lower Ordovician ironstones of the Iberian Massif (Zamora, Spain) and of the Armorican Massif (Central Brittany, France). *Journal of Sedimentary Research, Section A*, **68**, 53–62.

Ferrage E., Martin F., Micoud P., Petit S., de Parseval P., Beziat D. & Ferret J. (2003) Cation site distribution in clinochlores: a NIR approach. *Clay Minerals*, **38**, 329–338.

Fritsch E. & Rossman G.R. (1987) An update on color in gems. Part I: introduction and colors caused by dispersed metal ions. *Gems & Gemmology*, **23**, 126–139.

Fritsch E. & Rossman G.R. (1988) An update on color in gems. Part II: colors involving multiple atoms and color centers. *Gems & Gemmology*, **24**, 3–15.

Gloaguen E., Branquet Y., Boulvais P., Moëlo Y., Chauvel J.-J., Chiappero P.-J. & Marcoux E. (2007) Palaeozoic oolitic ironstone of the French Armorican Massif: a chemical and structural trap for orogenic base metal–As–Sb–Au mineralization during Hercynian strike-slip deformation. *Mineralium Deposita*, **42**, 399–422.

Hey M.H. (1954) A new review of the chlorites. *Mineralogical Magazine*, **30** (224), 277–291.

Hillier S. & Velde B. (1991) Octahedral occupancy and the chemical composition of diagenetic (low-temperature) chlorites. *Clay Minerals*, **26**, 149–168.

Inoué S. & Kogure T. (2016) High-resolution transmission electron microscopy (HRTEM) study of stacking irregularity in Fe-rich chlorite from selected hydrothermal ore deposits. *Clays and Clay Minerals*, **64**, 131–144.

Ito J. (1965) Synthesis of vanadium silicates: haradaite, goldmanite and roscoelite. *Mineralogical Journal*, **4**, 299–316.

Jiang W.-T., Peacor D.R. & Slack J.F. (1992) Microstructures, mixed layering, and polymorphism of chlorite and retrograde berthierine in the Kidd Creek massive sulfide deposit, Ontario. *Clays and Clay Minerals*, **40**, 501–514.

Joo I.-D. & Lee B.-H. (2010) Effect of V-doping on colour and crystallization of malayaite pigments. *Journal of the Korean Ceramic Society*, **47**, 302–307.

Kompanchenko A.A., Voloshin A.V. & Balagansky V.V. (2018) Vanadium mineralization in the Kola region, Fennoscandian Shield. *Minerals*, **8**(11), 474.

Leach D.L., Taylor R.D., Fey, D.L., Diehl, S.F. & Saltus, R.W. (2010) A deposit model for Mississipi Valley-type lead–zinc ores. Chapter A in: *Mineral Deposit Models for Resource Assessment*. USGS Scientific Investigation Reports 2010-5070-A. US Geological Survey, Reston, VA, USA.

Mathian M., Hebert B., Baron F., Petit S., Lescuyer J.-L., Furic R. & Beaufort D. (2018) Identifying the phyllosilicates of hypogene ore deposits in lateritic saprolites using the near-IR vspectroscopy second derivative methodology. *Journal of Geochemical Exploration*, **186**, 298–314.

Mattson S.M. & Rossman G.R. (1987) Identifying characteristics of charge transfer transitions in minerals. *Physics and Chemistry of Minerals*, **14**, 94–99.

McOnie A.W., Fawcett J.J. & James R.S. (1975) The stability of intermediate chlorites of the clinochlore–daphnite series at 2 Kbar *P*H₂O. *American Mineralogist*, **60**, 1047–1062.

Mellini M., Nieto F., Alvarez F. & Gomez-Pugnaire M.-T. (1991) Mica-chlorite intermixing and altered chlorite from the Nevado-Filabride micaschists, southern Spain. *European Journal of Mineralogy*, **3**, 27–38.

Mesto E, Scordari F, Lacalamita M & Schingaro E (2012) Tobelite and NH₄⁺-rich muscovite single crystals from Ordovician Armorican sandstones (Brittany, France): structure and crystal chemistry. *American Mineralogist*, **97**, 1460–1468.

Meunier J.D. (1994) The composition and origin of vanadium-rich clay minerals in Colorado Plateau Jurassic sandstones. *Clays and Clay Minerals*, **42**, 391–401.

Moëlo Y., Gloaguen E., Lulzac, Y. & Le Roch P. (2006) Minéralogie du gisement de Saint-Aubin-des-Châteaux (Loire-Atlantique). *Cahier des Micromonteurs*, **91**, 3–25.

Moëlo Y., Lasnier B., Palvadeau P., Léone P. & Fontan F. (2000) La lulzacite, Sr₂Fe²⁺(Fe²⁺,Mg)₂Al₄(PO₄)₄(OH)₁₀, un nouveau phosphate de strontium (Saint-Aubin-des-Châteaux, Loire-Atlantique, France). *Comptes Rendus de l'Académie des Sciences, Sciences de la Terre et des Planètes*, **330**, 317–324.

Moëlo Y., Lulzac Y., Rouer O., Palvadeau P., Gloaguen E. & Léone P. (2002) Pretulite with Sc-bearing zircon and xenotime from a paleozoic sedimentary iron ore (Saint-Aubin-des-Châteaux, Armorican Massif, France). *Canadian Mineralogist*, **40**, 1657–1673.

Moëlo Y., Rouer O. & Bouhnik-Le Coz M. (2008) From diagenesis to hydrothermal recrystallization: Mineralogy and chemistry of polygenic Sr-rich fluorapatite from the oolitic ironstone of Saint-Aubin-des-Châteaux (Armorican Massif, France). *European Journal of Mineralogy*, **20**, 205–216.

Novak F., Velensky J., Losert J., Kupka F. & Valcha Z. (1959) Orthochamosite, a new mineral from hydrothermal ore veins of Kank near Kutna Hora (Kuttenberg), Czechoslovakia. *Geologie (Berlin)*, **8**, 159–167.

Olivier B. (2006) *The Geology and Petrology of the Merelani Tanzanite Deposit, NE Tanzania*. PhD thesis, University of Stellenbosch, South Africa, 322 pp.

Orcel J. (1923) Sur la bavalite de Bas-Vallon. *Comptes Rendus de l'Académie des Sciences*, **177**, 271–273.

Papike J.J., Simo S.B., Burge P.V., Bell A.S., Shearer C.K. & Karner J.M. (2016) Chromium, vanadium, and titanium valence systematics in solar system pyroxene as a recorder of oxygen fugacity, planetary provenance, and processes. *American Mineralogist*, **101**, 907–918.

Parra T., Vidal O. & Theye T. (2005) Experimental data on the Tschermak substitution in Fe-chlorite. *American Mineralogist*, **90**, 359–370.

Platonov A.N. (1976) *The Nature of the Colour of Minerals* (Naukova Dumka, editor). Institut Geochem. i Mineral., Akad. nauk Ukr. SSR, Kiev, Ukraine, 264 pp. (in Russian).

Platonov A.N., Langer K., Chopin C., Andrut M. & Taran N. (2000) Fe^{2+}–Ti^{4+} charge-transfer in dumortierite. *European Journal of Mineralogy*, **12**, 521–528.

Pochon A., Beaudoin G., Branquet Y., Boulvais P., Gloaguen E. & Gapais D. (2017) Metal mobility during hydrothermal breakdown of Fe–Ti oxides: insights from Sb–Au mineralizing event (Variscan Armorican Massif, France). *Ore Geology Reviews*, **91**, 66–99.

Pochon A., Branquet Y., Gloaguen E., Ruffet G., Poujol M., Boulvais P. *et al.* (2019) A Sb ± Au mineralizing peak at 360 Ma in the Variscan belt. *Bulletin de la Société Geologique de France*, **190**, 4.

Pochon A., Gapais D., Gloaguen E., Gumiaux C., Branquet Y., Cagnard F. & Martelet G. (2016a) Antimony deposits in the Variscan Armorican belt, a link with mafic intrusives? *Terra Nova*, **28**, 138–145.

Pochon A., Gloaguen E., Branquet Y., Poujol M., Ruffet G., Boiron M.-C. *et al.* (2018) Variscan Sb–Au mineralization in Central Brittany (France): a new metallogenic model derived from the Le Semnon district. *Ore Geology Reviews*, **97**, 109–142.

Pochon A., Poujol M., Gloaguen E., Branquet Y., Cagnard F., Gumiaux C. & Gapais D. (2016b) U–Pb LA-ICP-MS dating of apatite in mafic rocks: evidence for a major magmatic event at the Devonian–Carboniferous boundary in the Armorican Massif (France). *American Mineralogist*, **101**, 2430–2442.

Povar I., Spinu O., Zinicovscaia I., Pintile B. & Ubaldini S. (2019) Revised Pourbaix diagrams for the vanadium–water system. *Journal of Electrochemical Science and Engineering*, **9**, 75–84.

Richardson S.M. & Richardson J.W. (1982) Crystal structure of a pink muscovite from Archer's Post, Kenya: implications for reverse pleochroism in dioctahedral micas. *American Mineralogist*, **67**, 69–75.

Rule A.C. & Bailey S.W. (1987) Refinement of the crystal structure of a monoclinic ferroan clinochlore. *Clays and Clay Minerals*, **35**, 129–138.

Shau Y.-H. & Peacor D.R. (1992) Phyllosilicates in hydrothermally altered basalts from DSDP Hole 504B, Leg 83 – a TEM and AEM study. *Contributions to Mineralogy and Petrology*, **112**, 119–133.

Shirozu H. & Bailey S.W. (1965) Chlorite polytypism: III. Crystal structure of an orthohexagonal iron chlorite. *American Mineralogist*, **50**, 868–885.

Smyth J.R., Darby Dyar M., May H.M., Bricker O.P. & Acker J.G. (1997) Crystal structure refinement and Mössbauer spectroscopy of an ordered triclinic clinochlore. *Clays and Clay Minerals*, **45**, 544–550.

Takeno N. (2005) *Atlas of Eh–pH Diagrams. Intercomparison of Thermodynamic Databases*. Open file report 419. Geological Survey of Japan, Tokyo, Japan, 287 pp.

Tartèse R., Poujol M., Gloaguen E., Boulvais P., Drost K., Košler J. & Ntaflos T. (2015) Hydrothermal activity during tectonic building of the Variscan orogen recorded by U–Pb systematics of xenotime in the Grès-Armoricain formation, Massif Armoricain, France. *Mineralogy and Petrology*, **109**, 2468–2483.

Trincal V. & Lanari P. (2016) Al-free di-trioctahedral substitution in chlorite and a ferri-sudoite end-member. *Clay Minerals*, **51**, 675–689.

Trincal V., Lanari P., Buatier M., Lacroix B., Charpentier D., Labaume P. & Muňoz M. (2015) Temperature micro-mapping in oscillatory-zoned chlorite: application to study of a green-schist facies fault zone in the Pyrenean Axial Zone (Spain). *American Mineralogist*, **100**, 868–885.

Uher P., Kováčik M., Kubiš M., Shtukenberg A. & Ozdín D. (2008) Metamorphic vanadian–chromian silicate mineralization in carbon-rich amphibole schists from the Malé Karpaty Mountains, Western Carpathians, Slovakia. *American Mineralogist*, **93**, 63–73.

Vidal O., De Andrade V., Lewin E., Muñoz M., Parra T. & Pascarelli S. (2006) P–T–deformation–Fe^{3+}/Fe^{2+} mapping at the thin section scale and comparison with XANES mapping: application to a garnet-bearing metapelite from the Sambagawa metamorphic belt (Japan). *Journal of Metamorphic Geology*, **24**, 669–683.

Walker J.R. & Bish D.L. (1992) Application of Rietveld refinement techniques to a disordered IIb Mg-chamosite. *Clays and Clay Minerals*, **40**, 319–322.

Whitney G. & Northrop H.R. (1986) Vanadium chlorite from a sandstone-hosted vanadium–uranium deposit, Henry basin, Utah. *Clays and Clay Minerals*, **34**, 488–495.

Wiewióra A. & Weiss Z. (1990) Crystallochemical classifications of phyllosilicates based on the unified system of projection of chemical composition: II. The chlorite group. *Clay Minerals*, **25**, 81–92.

Zanazzi P.F., Montagnoli M., Nazzareni S. & Comodi P. (2006) Structural effects of pressure on triclinic chlorite: a single-crystal study. *American Mineralogist*, **91**, 1871–1878.

Zane A., Sassi R. & Guidotti C.V. (1998) New data on metamorphic chlorite as a petrogenetic indicator mineral, with special regard to greenschist-facies rocks. *Canadian Mineralogist*, **36**, 713–726.

Zheng H. & Bailey S.W. (1989) The structures of intergrown triclinic and monoclinic II-b chlorites from Kenya. *Clays and Clay Minerals*, **37**, 308–316.